JOURNAL OF GEOPHYSICAL RESEARCH, VOL. 113, E12002, doi:10.1029/2008JE003181, 2008



# Relative age of interior layered deposits in southwest Candor Chasma based on high-resolution structural mapping

Chris H. Okubo,[1,2] Kevin W. Lewis,[3] Alfred S. McEwen,[1] and Randolph L. Kirk[2]

Received 1 May 2008; revised 29 June 2008; accepted 19 August 2008; published 2 December 2008.

[1] High-resolution topography generated from stereo HiRISE (High-Resolution Imaging Science Experiment) imagery reveals the meter-scale structure of interior layered deposits (ILD) in southwest Candor Chasma. This study seeks to determine the age of the local ILD relative to any normal faults that can be attributed to chasma formation. The study area is located near the contact of these ILD and the wall rock and is in an area where chasma-forming normal faults have been proposed. We find that while normal faults are found in the study area, these faults are not sufficiently large nor appropriately located or oriented to accommodate the roughly northeast-southwest extension that is required for normal faults that can be attributed to chasma formation. Additionally, bedding exposed in the local ILD generally dips toward the center of Candor Chasma, consistent with sediment deposition in a preexisting basin. Further, pit craters of Tithonia Catena, presumed to predate or be contemporaneous with the formation of west Candor Chasma, do not cut into the ILD within the study area. These independent lines of evidence support a postchasma age for the ILD exposed within the study area. Chasma-related normal faults may exist within these ILD at depth but are not exposed at the surface. Approximately 2 km of conformable stratigraphy is exposed in the study area, and therefore at least several kilometers of the local ILD were deposited subsequent to any chasma-related normal faulting that may have occurred in this part of Candor Chasma.

**Citation:** Okubo, C. H., K. W. Lewis, A. S. McEwen, and R. L. Kirk (2008), Relative age of interior layered deposits in southwest Candor Chasma based on high-resolution structural mapping, *J. Geophys. Res.*, *113*, E12002, doi:10.1029/2008JE003181.

## 1. Introduction

[2] A fundamental issue in Mars geology today is the relative timing between the formation of Valles Marineris and the accumulation of light toned layered deposits that are exposed within its chasma. Light toned layered deposits are common throughout the equatorial regions of Mars [e.g., *Schultz and Lutz*, 1988; *Malin and Edgett*, 2000; *Hynek et al.*, 2003]. In Valles Marineris, the light toned layered deposits are commonly referred to as the interior layered deposits (ILD) [e.g., *Lucchitta et al.*, 1992, 1994; *Schultz*, 1998a; *Lucchitta*, 1999; *Weitz et al.*, 2003]. The ILD are found in most, but not all, chasma of Valles Marineris, as well as in the peripheral chasma such as Hebes, Juventae and Ganges [*Scott and Tanaka*, 1986; *Witbeck et al.*, 1991].

[3] A large body of work has been dedicated to unraveling the geologic processes that may have led to the formation of the ILD [e.g., *Witbeck et al.*, 1991; *Lucchitta et al.*, 1992, 1994; *Chapman and Tanaka*, 2001; *Komatsu et al.*, 2004; *Mangold et al.*, 2008]. Much research has also been directed toward understanding the coupled structural evolution of the ILD and Valles Marineris at the scale of hundreds of meters to thousands of kilometers [e.g., *Lucchitta and Bertolini*, 1989; *Peulvast and Masson*, 1993a; *Lucchitta et al.*, 1994; *Schultz*, 1998b].

[4] The purpose of this work is to expand the current state of knowledge on the structure of the ILD and to understand the implications of this new information on the broader geologic evolution of Valles Marineris. We present observations on the meter to decameter-scale structure of the ILD based on high-resolution imagery and digital elevation models derived from stereo High-Resolution Imaging Science Experiment (HiRISE) [*McEwen et al.*, 2007] observations in southwest Candor Chasma (Figure 1). Our findings allow for previous interpretations of the structure and history of the ILD in the study area to be tested and further refined at length scales that are more than an order of magnitude smaller than was possible with earlier orbiter-based data sets.

[5] There are two basic interpretations of the relative timing for the deposition of the ILD and the formation of the chasmata of Valles Marineris. Evidence that the ILD predates formation of the chasmata has been previously reported [*Malin and Edgett*, 2000, 2001; *Montgomery and Gillespie*, 2005; *Catling et al.*, 2006]. These authors point to lines of evidence such as the presence of layered materials

[1]Lunar and Planetary Laboratory, Department of Planetary Sciences, University of Arizona, Tucson, Arizona, USA.
[2]U.S. Geological Survey, Flagstaff, Arizona, USA.
[3]Division of Geological and Planetary Sciences, California Institute of Technology, Pasadena, California, USA.


0148-0227/08/2008JE003181$09.00

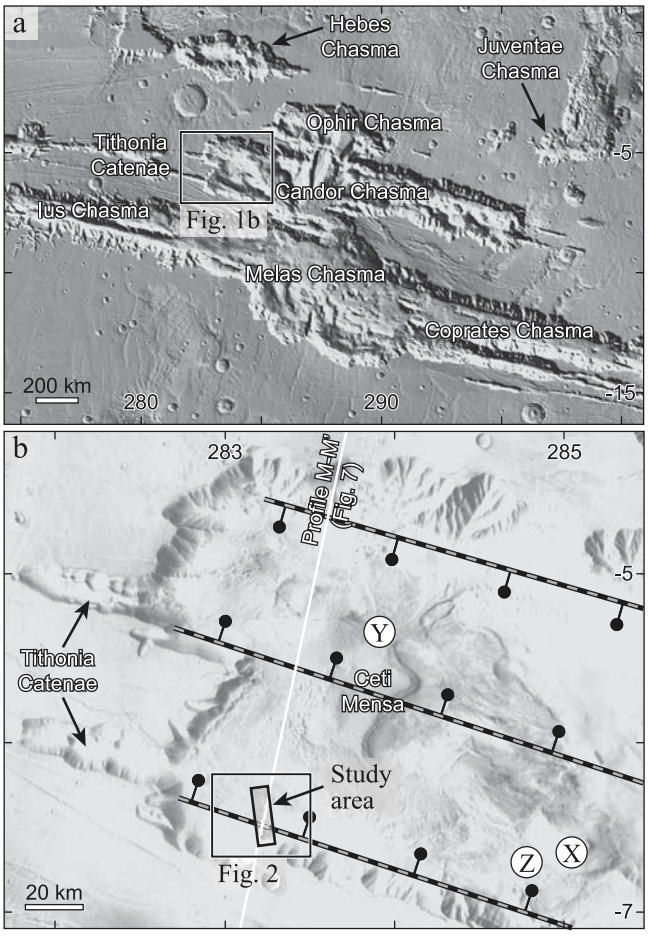


**Figure 1.** Location maps of the study area. (a) The major chasma in the central Valles Marineris region. Base map is MOLA shaded relief, with illumination from the north. (b) Location of the study area in southwest Candor Chasma. Dashed lines show the locations of chasma-forming normal faults predicted by *Schultz and Lin* [2001]. Bar and ball symbols are on the hanging wall side of each fault. Also shown are the locations of previous related studies in this area as referred to in this paper: X, *Fueten et al.* [2006]; Y, *Fueten et al.* [2007, 2008]; and Z, *Lucchitta* [2000] and *Chapman and Tanaka* [2001].

in the spurs and ravines of the chasmata walls and other superposition relationships in support of the interpretation that the chasmata formed by cutting into a Noachian-aged bedrock of ILD and its Hesperian-aged cover of plains materials. Alternately, the ILD have been interpreted to be Hesperian to Amazonian-aged materials that accumulated on top of Noachian-aged bedrock after, and perhaps during, the formation of the chasma. Evidence for a postchasma age for the ILD comes from diverse lines of study including geomorphology [*Lucchitta*, 1990; *Lucchitta et al.*, 1992; *Peulvast and Masson*, 1993a; *Chapman and Tanaka*, 2001; *Weitz et al.*, 2001; *Hynek et al.*, 2003; *Lucchitta*, 2008], geologic mapping [*Scott and Tanaka*, 1986; *Witbeck et al.*, 1991, *Lucchitta et al.*, 1994; *Schultz*, 1998a; *Lucchitta*, 1999], and structural analysis [*Peulvast and Masson*, 1993b; *Schultz*, 1998b; *Fueten et al.*, 2007, 2008]. Some spurs and ravines within the chasma walls have been interpreted to predate ILD deposition [e.g., *Peulvast and Masson*, 1993a; *Peulvast et al.*, 2001], contrary to the interpretations that similar landforms postdate ILD deposition [e.g., *Malin and Edgett*, 2000, 2001].

[6] While aspects of both interpretations may be true for different study areas, interpretations of a generally post-chasma age for the ILD have gained popular, but by no means overwhelming, support. Although many such interpretations of the geologic evolution of the ILD and Valles Marineris vary according to the specifics of the sites and types of data analyzed, a general framework has emerged [e.g., *Lucchitta and Bertolini*, 1989; *Peulvast and Masson*, 1993a; *Mège and Masson*, 1996; *Peulvast et al.*, 2001; *Lucchitta et al.*, 1994 *Schultz*, 1998b; and references therein]. Taken together, these previous works generally envisage a roughly three-phase evolution for Valles Marineris and the ILD; the phases are as follows:

[7] 1. During the Late Noachian to Early Hesperian, the growth of Syria Planum drove the radial emplacement of dikes, and related graben and pit craters, in the future region of Valles Marineris.

[8] 2. During or after the Early Hesperian, irregularly shaped ancestral basins (such as Hebes Chasma) formed through subsidence that was superimposed on the earlier Syria radial dikes, graben and pit craters. This subsidence may have been related to melting of subsurface water and formation of chaotic terrain. The ILD subsequently formed in these ancestral basins under depositional conditions that were subaerial, subaqueous, or a combination of both.

[9] 3. During the Amazonian, regional rift systems developed in the area of the ancestral basins and ILD. These rifts contributed to the formation of the Coprates north Melas-Ius Chasmata system superimposed on the Melas ancestral basin. Rifting also resulted in the Ophir north Candor Chasmata cutting through the Candor ancestral basin. Formation of these rift systems may have been driven by Tharsis-related stresses and may have been structurally influenced by the presence of the Early Hesperian (Syria radial) dike system and the ancestral basins. These rifts may have also connected the ancestral basins with one another and thereby facilitated draining of any extant bodies of water within them. Erosion (including landslides) subsequently widened the ancestral basins and rifts to their present-day form.

[10] These interpretations of the geologic history of the ILD and chasmata imply structural relationships that can be tested using data with sufficiently high spatial sampling. One important constraint on these interpretations is the orientation of the layers in the wall rock of the chasmata and in the ILD. Topographic and morphologic information on these layers at sufficient resolution has been collected from Mars Orbiter Laser Altimeter (MOLA), Mars Orbiter Camera (MOC) and the High-Resolution Stereo Camera (HRSC) data and examined in detail in previous studies.

[11] In a study of layer orientations of the upper wall rock of several chasmata in Valles Marineris, *Fueten et al.* [2005] show that the wall rock generally dips toward the center of the chasmata. These measurements are near to or at the proposed ancestral basins of Candor, Gangis, Capri and south Coprates. *Fueten et al.* [2005] interpret these findings to be evidence of subsidence related to the formation of these ancestral basins. In their study, the topographic

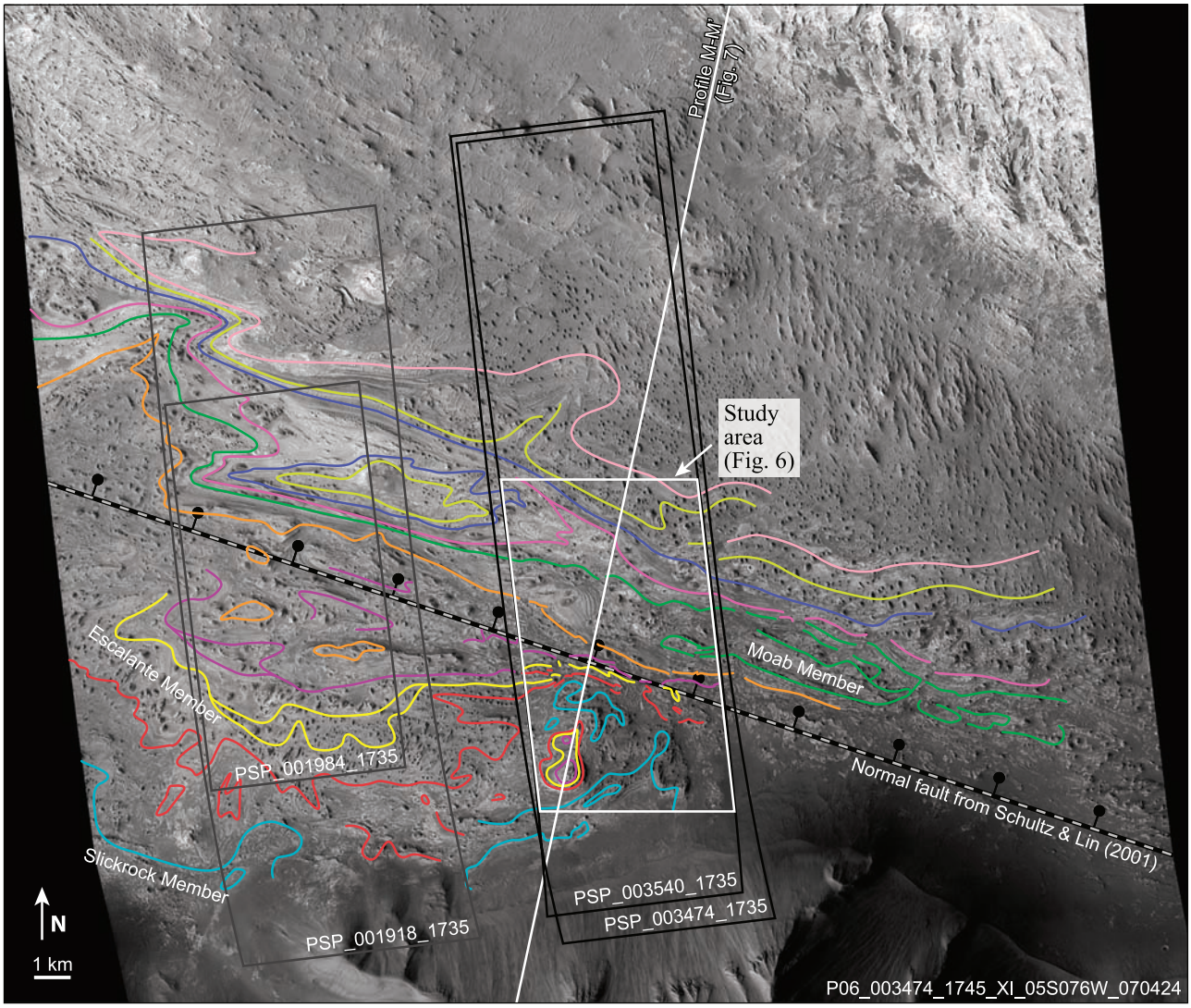


**Figure 2.** Context map showing the location of the study area and the full stereo HiRISE coverage. Also shown is an adjacent stereo HiRISE image pair. Base map is a CTX image (5 m/pixel). Structures interpreted in the study area are checked for consistency against the overlapping CTX image, as well as both HiRISE stereo pair coverage. Also shown are the traces of stratigraphic members and their relative ages as identified in this study. Key stratigraphic members are given provisional names to aid in their discussion.

information is from MOLA gridded data (128 pixels/degree, *ca.* 463 m/pixel), and the measured layers are resolved in MOC wide-angle (250 m/pixel) and narrow-angle (1.5–10 m/pixel) imagery coregistered to MOLA. Layer orientations are calculated from a manually selected set of topographic points along the same layer. The best fit plane to these points is calculated using a multilinear regression routine implemented in the commercial software Orion (http://www.pangaeasci.com). Layer orientations are calculated from data collected along layer trace lengths of 7.7 km to 32.6 km.

[12] In a subsequent study, *Fueten et al.* [2006] examined the dip of the ILD at the contact with the wall rock of south central Candor Chasma (location X in Figure 1b). Their measurements show that bedding in the ILD roughly parallels local topographic slope, that is, bedding dips away from the peak of the mounds and is subhorizontal in the surrounding plains. This pattern of layer orientations is interpreted to reflect draping of the ILD over preexisting topography such as basement fault blocks and erosional unconformities within the ILD. *Fueten et al.* [2006] find no evidence of syntectonic deposition of the ILD. Further, they see no evidence of large-scale normal faulting of the ILD as would be expected if the chasma formed through fault slip within the ILD. The majority of their measurements are of layers in the AHire (resistant, mesa-forming material that predates rifting) and AHil (layered material exposed along mesa slopes; older than AHire) units of *Lucchitta* [1999]. The data used for this study include a HRSC digital terrain model (DTM) constructed with 150 m postings and a 25 m/pixel panchromatic HRSC image. Layer orientations are based on topographic data collected along 0.8 to 14.5 km trace lengths and calculated using the Orion software.

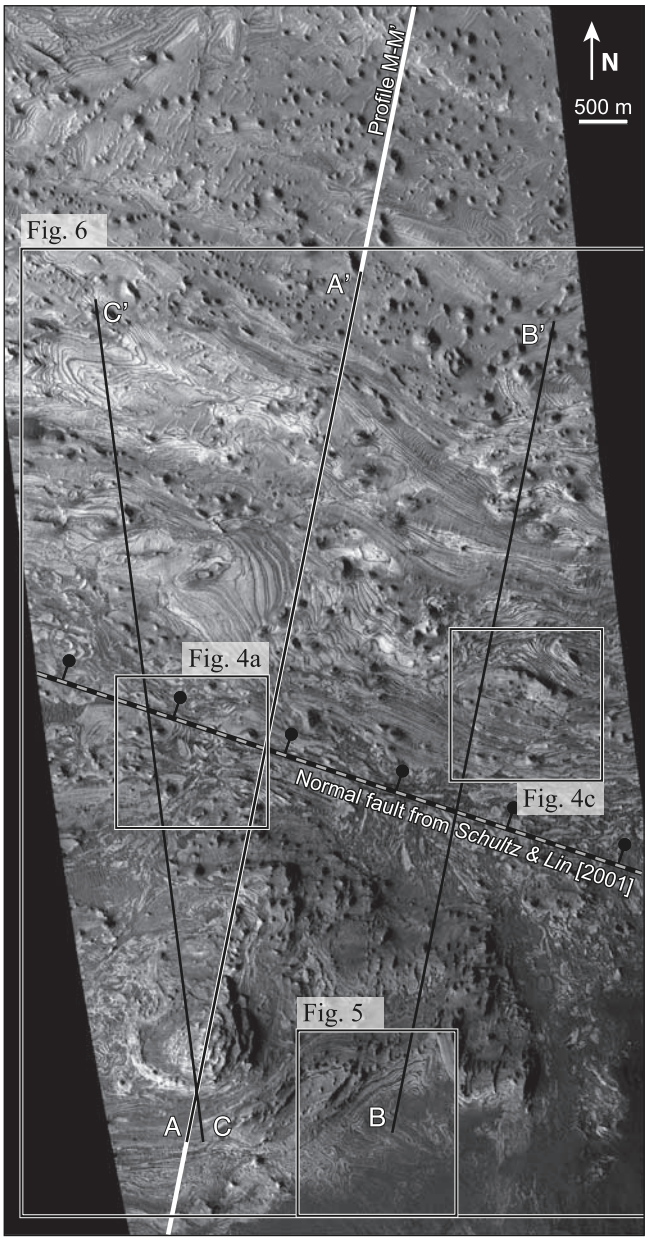


**Figure 3.** A subsection of HiRISE image PSP_003474_1735; one image in the stereo pair used in this study. Locations of other figures that show HiRISE imagery, as well as the structure map (Figure 6) are shown. Also shown are the locations of the profiles in Figure 7. Profiles A-A′ and M-M′ are coincident. Illumination is from the left.

[13] Similar correlations of layer dip and topography are observed in the ILD of Ophir Chasma by *Zegers et al.* [2006], in the ILD of Hebes Chasma by *Hauber et al.* [2006], in ILD of Iani Chaos by *Sowe et al.* [2007] and in a perched lens of ILD in north Coprates Chasma [e.g., *Schultz*, 1991] by *Hamelin et al.* [2008]. These studies use HRSC DTMs and THEMIS, MOC and HiRISE imagery and calculate layer orientations using a similar methodology as *Fueten et al.* [2005].

[14] In west Candor Chasma, *Fueten et al.* [2007, 2008] measure the orientations of the ILD in Ceti Mensa (location Y in Figure 1b). A HRSC DTM (50 m postings) and multispectral image (12.5 m/pixel) are analyzed using similar techniques as *Fueten et al.* [2005]. They propose that Ceti Mensa is composed of ILD that were deposited in the Candor ancestral basin and then faulted during the formation of Valles Marineris. Sulfate-bearing sediments subsequently blanketed these fault-bounded blocks of ILD during the latter stages of rifting.

[15] These interpretations of the history of the ILD and Valles Marineris can be tested with higher-resolution topographic data and structural mapping at length scales of 100 m or less. While previous interpretations imply many corollaries, there are several fundamental and tractable tests that can be conducted at this scale. If the ILD are (ancestral) basin-filling sediments, they should show on-lap relationships with the wall rock of the chasma. Further, evidence of syntectonic deposition [e.g., *Sharp et al.*, 2000] would be expected if sedimentation were contemporaneous with rifting. Also, the ILD should show evidence of normal faulting if rifting occurred in the ancestral basins after ILD deposition, assuming negligible postdeformation sediment cover. The motivation of this paper is to use such corollaries to test previous interpretations of the structural history of the ILD and southwest Candor Chasma using a high-resolution DTM derived from stereo HiRISE observations.

## 2. Southwest Candor Chasma Study Area

[16] A HiRISE stereo observation in the far southwest part of Candor Chasma is well placed for testing interpretations of the timing between accumulation of the local ILD and formation of the chasma. The stereo pair consisting of PSP_003474_1735 and PSP_003540_1735 is centered at −6.433°N, 283.216°E (planetocentric) and crosses the topographic low (or "moat") near the contact between the local ILD and wall rock (Figures 1 and 2). The site is along strike of the southern pit chain of the Tithonia Catenae and crosses the west end of fault 5 of *Schultz and Lin* [2001], near their profile b. The site is also roughly 45 km southwest of the peak of Ceti Mensa. The layered materials exposed within the study area are classified as eroded massive material (Avme) in the map of *Witbeck et al.* [1991].

[17] The HiRISE DTM used in this study is generated following the method of *Kirk et al.* [2008]. The freely available Integrated Software for Imagers and Spectrometers image processing routines (http://isis.astrogeology.usgs.gov) and the commercial Socet Set image analysis software (http://www.socetset.com) are used to process the HiRISE stereo observations into a DTM. The HiRISE data are available from NASA's Planetary Data System Imaging Node (http://pds-imaging.jpl.nasa.gov). Observations PSP_003474_1735 (0.275 m/pixel) and PSP_003540_1735 (0.264 m/pixel) are combined to produce a DTM with elevation postings at every 1 m. With a stereo convergence angle of 25°, 0.275 m/pixel in the more oblique image, and assuming 1/5 pixel correlations, the vertical precision is 0.275/5/tan(25) = 0.12 m. In rough areas or steep slopes, the precision is most limited by the 1 m postings.

[18] Detailed structural mapping is focused on a 5.27 km by 8.53 km subsection of the full DTM, which spans 5.27 km by 21.11 km (Figure 3). The DTM is being mapped in

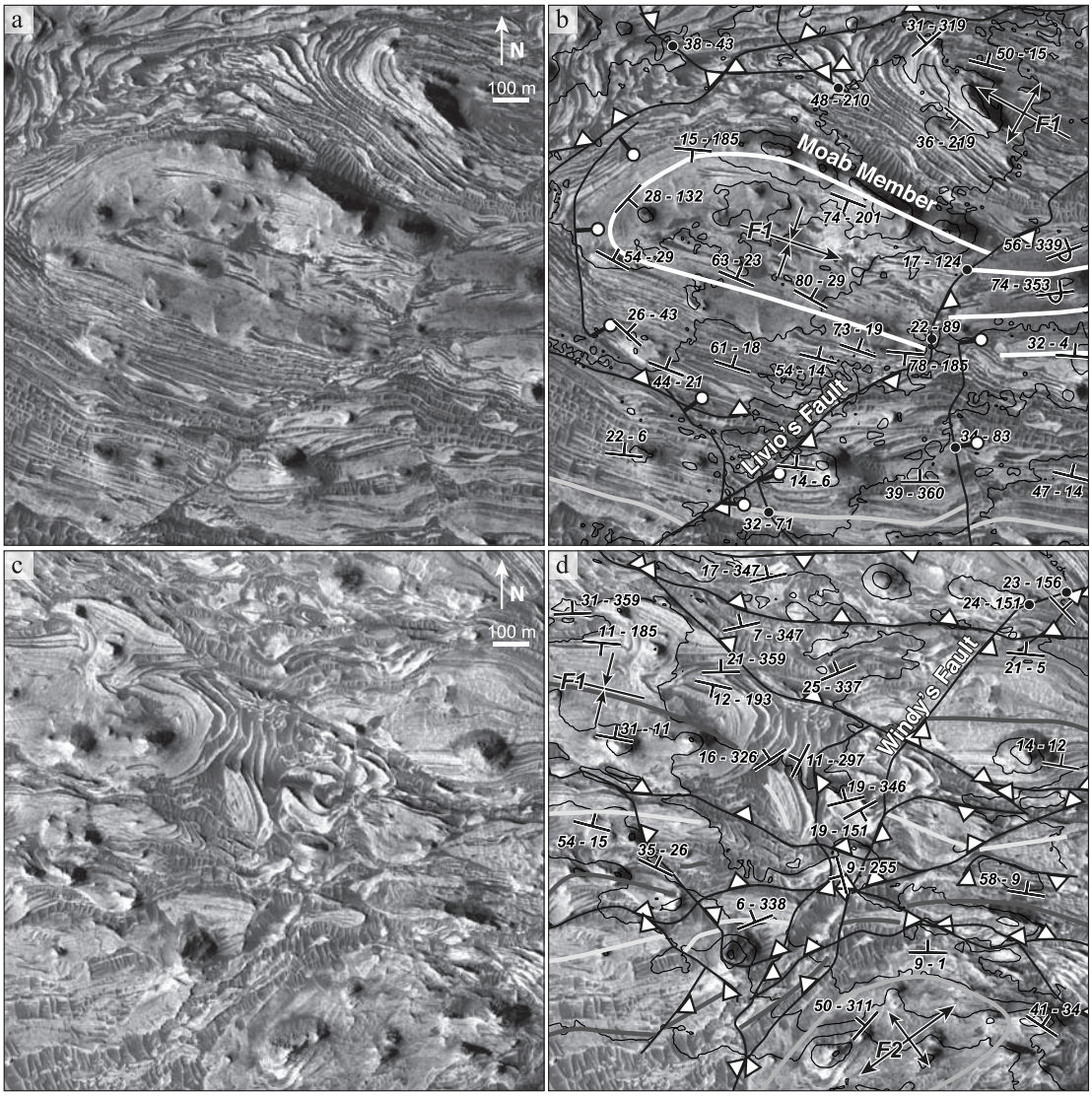


**Figure 4.** Examples of structures discussed in the text. (a) Image and (b) structural interpretations of folds and faults. Stratigraphic members, delineated with thick lines, are roughly 100 m thick and massive. (c) Image and (d) structural interpretations of fragmented blocks of layered deposits. Bedding within each block is conformable but is not continuous across blocks. Dark regions between blocks are filled with sand. Illumination is from the left in all images. See Figure 6 for color version and description of symbols.

subsections in order to maintain manageable file sizes. The subsection discussed here contains the majority of the scene's structural diversity, and interpretations drawn from these findings are checked for consistency against preliminary observations from adjacent areas covered by HiRISE and Context Camera (CTX) [*Malin et al.*, 2007] data (Figure 2).

[19] Structural mapping is focused on quantifying the orientations of layers, faults and folds within these ILD. Following *Fueten et al.* [2005] and others, layer and fault orientations are calculated using the Orion structural analysis software. Faults and layers are identified in PSP_003540_1735 and their orientations are calculated using trace lengths of *ca.* 75 m to 150 m. Thus structural orientations are effectively resolved at length scales on the order of 100 m. Measurements of structural attitudes at smaller scales are hindered by the presence of boulders, sand dunes, and variability in the planarity of the layers and faults. Repeated measurements also show that *ca.* 100 m is in general a reliable length scale for repeatable measurements of structural attitudes in this DTM. High-frequency topography inhibits reliable measurements at length scales less than roughly 50–75 m, depending on scene content. For the set of fault and layer measurements presented here, the average error in dip is 5.2° and the average error in dip direction is 19.4°. Measured orientations with either a dip error greater than the dip angle (for dips > 5°) or a dip direction error greater than 30° are excluded from this study.

## 3. Results

[20] HiRISE imagery reveals that the layers of the ILD are extensively folded and faulted in the study area (Figures 3–5). Measurements of bedding orientation taken in areas of minimal faulting and folding reveal that the layers

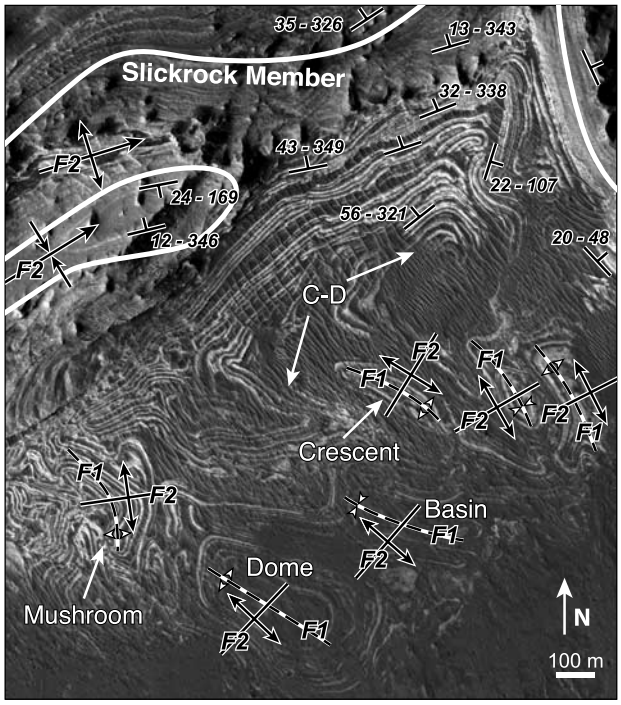


**Figure 5.** Examples of superimposed folds in the south part of the study area. Dome-basin, dome-crescent-mushroom, and concordant-discordant (C-D) interference patterns [cf. *Ramsay and Huber*, 1987] are observed. These folds indicate a transition from an initial northeast-southwest shortening direction (F1 folds) to a roughly northwest to southeast directed shortening (F2 folds), which is broadly coincident with the maximum strain directions (Figures 6 and 7) of the thrust and normal fault populations. Illumination is from the left. See Figure 6 for color version and description of symbols.

generally dip to the north, toward the center of Candor Chasma (Figures 6–8). For clarity, only values of dip and dip direction for faults and representative bedding are labeled on Figure 6. All measured fault and bedding orientations are labeled in Figure S1 and plotted on Figure 8.[1] Further, only the faults for which the sense of displacement could be identified are outlined Figures 6 and S1. There are numerous fault-like structures that are not outlined because they have insufficient or ambiguous information that precludes determining their sense of offset.

[21] Measurements of true thickness for individual layers are calculated from apparent thickness as measured in the map-projected HiRISE image and the dip of the layers (compare dips labeled in Figure S1) in areas where these layers are not faulted. The majority of the layers are found to be *ca.* 5 m thick. Interspersed among these thinner layers are massive to weakly bedded layers that are generally *ca.* 100 m thick (Figures 4a, 4b, and 6). The entire stratigraphic sequence of layered deposits exposed in Figure 6 appears to be conformable, with the exception of a zone of discontinuous blocks of layered deposits in the midlatitudes of the study area (Figures 4c and 4d).

[22] Along section C-C′ (Figure 7), the ILD are found to constitute a stratigraphic section that has an apparent thickness of roughly 2 km. This value of apparent thickness has not been corrected for stratigraphic duplication because of faulting because the magnitude of fault strain has not yet been determined. Fault duplication of stratigraphy is however estimated to contribute less than 200 m to the apparent section thickness, given that most of these faults are short, and therefore have correspondingly small (meter-scale) displacements [cf. *Schultz et al.*, 2006]. Rigorous analysis of fault strain in this area is the topic of a subsequent paper.

[23] The 100 m thick layers are readily resolved on the overlapping CTX data (Figure 2). The CTX data reveal that these layers observed in the HiRISE image continue to outcrop for several 10s of km to the east and west of the study area. In this way, the 100 m thick layers provide an important link between the structures interpreted in the HiRISE data and the regional structural context provided by CTX (compare Figures 2 and 6). The 100 m thick layers are also useful stratigraphic markers that are used in this paper to illustrate structural interpretations in cross section (Figure 7). Thus given their importance, the 100 m thick layers are herein referred to as stratigraphic members (Figure 6). Significant members are given provisional names to aid in discussing interpreted structures. Structures interpreted in the HiRISE data are checked for consistency against the map-projected CTX image using these stratigraphic members.

[24] Numerous synclines and anticlines are identified throughout the study area. These appear to be largely the result of folding, as fault cores are not observed within these structures. A prominent overturned fold incorporating in the Moab Member is observed in the east-central part of the study area (Figures 4b and 6). Several broad folds are also expressed in stratigraphic units that are younger than the Moab Member. The majority of these folds have axes that trend roughly northwest-southeast, indicating a northeast-southwest oriented direction of maximum compressional strain (Figure 8).

[25] Several superimposed folds are observed in the south end of the study area (Figures 5 and 6). These folds are expressed in layers that lie below the Slickrock Member and thus deform the oldest exposed stratigraphic units in the study area. These folds show concordant-discordant, dome, basin, crescent and mushroom interference patterns [cf. *Ramsay and Huber*, 1987]. The orientations of these patterns indicate that the older folds have axes that trended roughly northwest-southeast, implying a northeast-southwest shortening direction. For simplicity, folds trending in this older, northwest-southeast orientation are hereafter referred to as the F1 folds (Figure 8). Axes of the younger folds (hereafter F2 folds) trend roughly northeast-southwest (Figure 8), corresponding to a roughly northwest to southeast shortening direction. This indicates a roughly sixty degree counterclockwise rotation in horizontal shortening between the first and second folding event. The F1 folds are observed throughout the study area, while the F2 folds are found only in the southern end of the study area.

[26] Numerous faults are also observed. The sense of slip along the mapped faults is determined from the sense of offset and measured orientations of crosscut bedding and other faults [e.g., *Suppe*, 1985]. The faults are found to have

[1] Auxiliary materials are available in the HTML. doi:10.1029/2008JE003181.

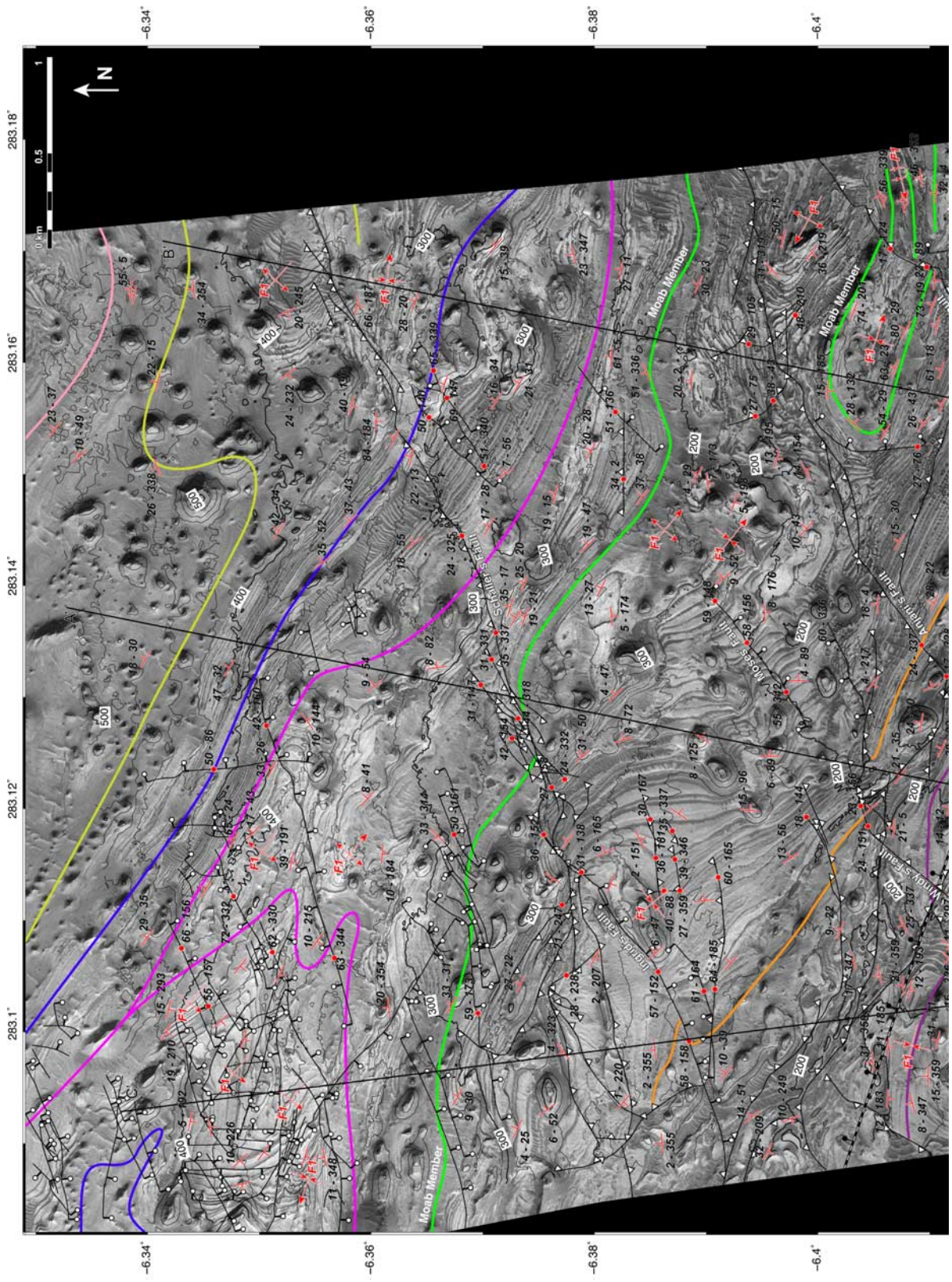


**Figure 6.** Reduced resolution structure map of the study area. Fault and bedding orientations are measured from the HiRISE DTM. Only strike and dip symbols are plotted here for clarity. Measured values of dip and dip direction and the full-resolution map are provided in Figure S1. Also shown are traces of identified stratigraphic members. Line color for each member corresponds to the line colors used in the context map (Figure 2) and profiles (Figure 7). The predicted location of a chasma-related normal fault from *Schultz and Lin* [2001] is indicated, although normal faults are not observed in that area. Illumination is from the left.

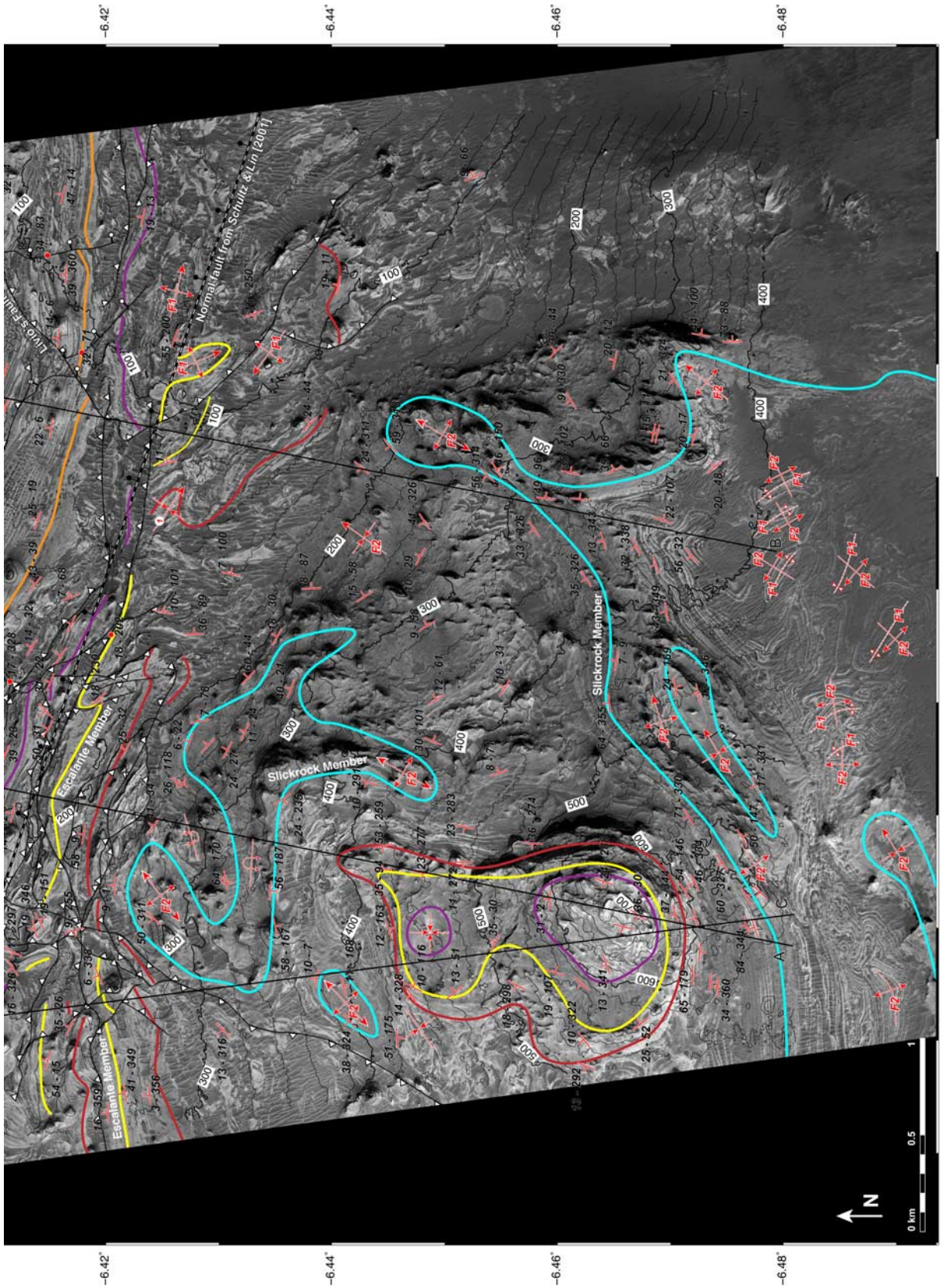


**Figure 6.** (continued)

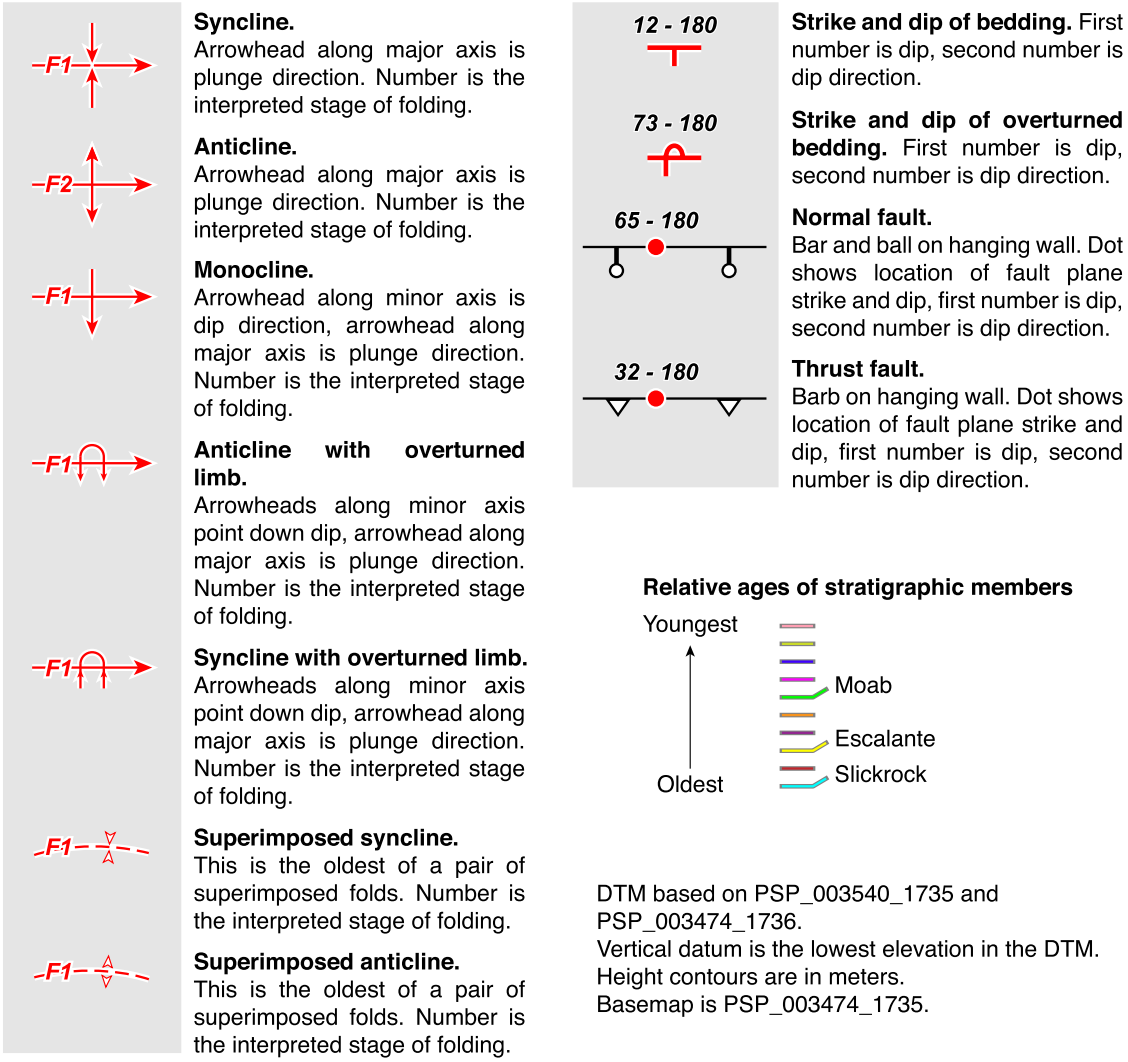


**Figure 6.** (continued)

either thrust or normal displacements (Figure 8). The thrust faults have an average dip angle of 31°, with a standard deviation of 11°, while normal faults have an average dip angle of 55°, also with a standard deviation of 11° (Tables 1a and 1b). Strike-slip faults [e.g., *Anguita et al.*, 2001] are not observed. Further, the HiRISE data are at a sufficiently high resolution to determine crosscutting relationships between the faults and folds. These results are plotted in Figure 6, which shows the locations of fault and layer orientation measurements, interpretations of these measurements and the locations of cross sections (Figure 7) that further illustrate our interpretations.

[27] Thrust faults are common within the midlatitudes of the study area, where they form networks of linked and mutually crosscutting faults. An extensive network of linked thrust faults is found to be the cause of the fragmented (nonconformable) layers that occur in the mid latitudes of the study area (e.g., Figure 4). Each fragment of layered deposits is a thrust-bounded fault block. This swath of fragmented layered materials extends across the width of the overlapping CTX image, implying that the network of thrust faults is equally extensive. Thrust faulting has resulted in repeated stratigraphic sequences in some areas, such as in the Escalante and adjacent members (Figure 6). While there is considerable scatter in the measured fault orientations, the maximum horizontal contraction accommodated by thrust faulting is found to be roughly oriented northwest-southeast, with a lesser amount of compression in the orthogonal northeast-southwest direction (Figure 8).

[28] Normal faults are found primarily within the northern half of the study area. These faults form isolated, linked, conjugate and graben-bounding geometries. Normal faults are mutually crosscutting, but are rarely mechanically linked along strike as the thrust faults commonly are. Thus unlike the thrust faults, normal faults do not form long and extensive interconnected arrays. The maximum observed length for a normal fault in the study area is 1.6 km (Ingrid's fault). Throughgoing normal faults or fault zones that span or exceed the width of the study area are not observed. Given the orientations of these normal faults (Figure 8), maximum horizontal extension is found to be roughly oriented northwest-southeast, with a minor component of horizontal extension in the orthogonal northeast-southwest direction. Thus the local direction of maximum extension as

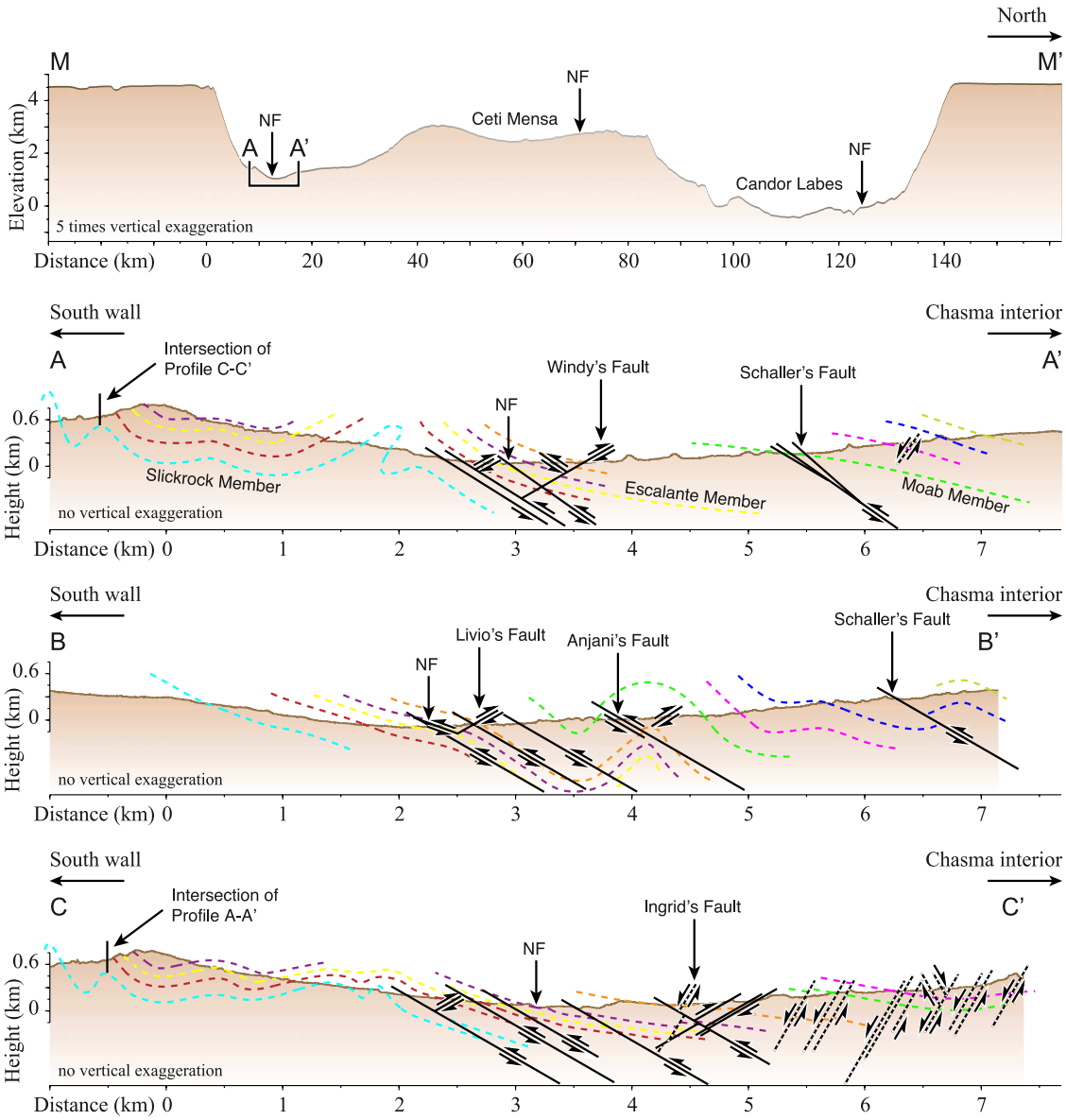


**Figure 7.** Topographic and interpreted structural profiles through the study area. Profile M-M′ shows the general location of this study area relative to the topography of Candor Chasma. Profiles A-A′ and M-M′ are coincident, and profiles A-A′ and C-C′ intersect as shown. Fault and bedding orientations are based on measured values and observed crosscutting relationships within approximately 500 m on either side of the profile. Predicted locations of chasma-related normal faults from *Schultz and Lin* [2001] are labeled NF. Chasma-related normal faulting is not observed or implied in the surface structure, and therefore such faults must be buried if present. The normal faults that are observed are too short in map length to be attributed to chasma-related faulting. Topography in profiles A-A′ to C-C′ are from the HiRISE DTM, while profile M-M′ uses MOLA elevations gridded at 128 pixels/°.

indicated by the orientations of these normal faults is subparallel with the orientation of maximum compression as indicated by the thrust faults. Note that the normal faults observed here are different from those studied by *Fueten et al.* [2007, 2008] (locations X and Y in Figure 1).

[29] Where crosscutting relationships are observed, there is a general pattern of relative age among the faults and folds. The F1 folds are generally the oldest deformational structures observed in the study area, followed in age by the normal and thrust faults. While not all faults and folds have unambiguous crosscutting relationships, these relative ages hold true in all clear instances. Additionally, the thrust faults generally crosscut and the normal faults, however crosscutting relationships are insufficient to establish the relative age of all intersecting faults. Crosscutting relationships between faulting and the F2 folds are not observed.

## 4. Discussion

[30] The mapped geometries of faults in the study area are an effective test of prior interpretations of the relative age of

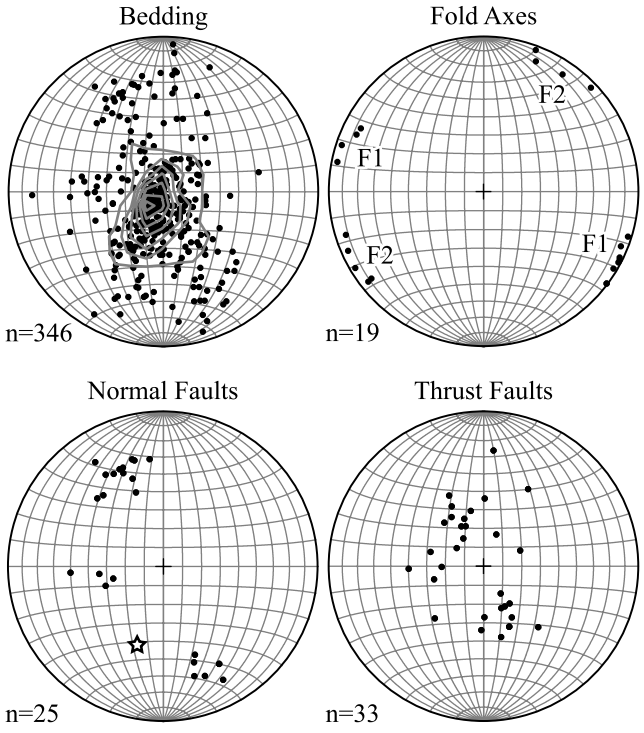


**Figure 8.** Orientations of all measured bedding, folds, and faults in the study area. Not all bedding and fault orientations can be measured because of noise in the DTM. Thus while these data do not completely represent both fault populations, these plots do show an overall sense of maximum strain aligned in a roughly northeast-southwest orientation. Star indicates the orientation of the chasma-related normal fault predicted by *Schultz and Lin* [2001]. The plot of bedding orientations includes all measurements taken within the study area; interval of area contours is 2% per 1% area. Plots utilize Schmidt equal area projection.

the local occurrences of ILD and chasma-related normal faulting. *Schultz and Lin* [2001] use numerical model inversion of MOLA topography to predict the locations of chasma-forming normal faults in the Valles Marineris region. Their best fit location of the southwest bounding fault for Candor Chasma is within our study area (e.g., Figure 2). However, our observations reveal that neither normal faults nor associated deformation band damage zones [e.g., *Okubo and Schultz*, 2005; *Okubo et al.*, 2008] occur at the surface in this location (Figure 6).

[31] Additionally, none of the normal faults that are observed within the study area, or within the overlapping HiRISE and CTX imagery, are long enough to be attributed to chasma formation. The normal faults that are observed in the study area are 1.6 km or less in length. Assuming a critical shear strain (displacement/length) of $6.7 \times 10^{-3}$ [*Wilkins et al.*, 2002] to $\sim 1 \times 10^{-2}$ [*Hauber et al.*, 2007] for normal faults on Mars, the longest normal fault in the study area (1.6 km) would have a maximum displacement of 11 m to 16 m – far less than the roughly 6 km of cumulative displacement [*Schultz and Lin*, 2001] required to form this part of Candor Chasma through normal faulting. Additionally, the major component of extension along the observed normal faults is oriented roughly orthogonal (northwest–southeast) to the direction of extension predicted by *Schultz and Lin* [2001] for chasma-related normal faulting. The average trend of the normal faults is 62°, compared to the roughly 110° trend of the normal fault predicted by *Schultz and Lin* [2001]. Thus if pervasive normal faulting did develop here as a part of chasma formation, such faults must predate deposition of the locally exposed ILD and are buried.

[32] Prominent chains of pit craters (Tithonia Catenae) extend to the west of this region of Candor Chasma (Figure 1). In the Valles Marineris area, pit chains such as these are interpreted to be the surface manifestations of dilational normal faults [*Wilkins and Schultz*, 2003], dikes [*Schultz*, 1998b] or tension fractures [*Tanaka and Golombek*, 1989], which may have influenced [*Schultz*, 1998b; *Lucchitta et al.*, 1994] or are genetically related to [*Tanaka and Golombek*, 1989; *Wilkins and Schultz*, 2003] formation of the chasma. While these catena embay the wall of southwest Candor Chasma, the HiRISE and CTX imagery show that pit craters do not continue into these ILD. Thus these pit chains, and any underlying fractures, are older than the local exposures of ILD. Therefore any activity along these fractures related to chasma formation must have occurred prior to the deposition of the local ILD. A pre-ILD age of the pit chains is consistent with previous interpretations that catena formation is related to Early Hesperian Syria radial dikes that predate the chasma [*Mège and Masson*, 1996].

[33] Bedding within the local ILD generally dips toward the center of the chasma in areas where these beds are not adjacent to prominent faults or folds (Figures 6–8). This orientation of bedding is consistent with deposition of these ILD within a preexisting or actively subsiding basin. A difficulty with these ILD being deposited in an actively subsiding basin is that, again, there is no evidence of normal faulting that can be attributed to subsidence of the chasma,

**Table 1a.** Measurements of Dip, Dip Direction, and Corresponding Errors for Normal Faults in the Study Area[a]

| Dip | Error | Dip Direction | Error | $\phi$ |
|---|---|---|---|---|
| 50° | 5.1° | 86° | 6.4° | 10° |
| 50° | 6.4° | 161° | 6.0° | 10° |
| 50° | 4.2° | 140° | 6.5° | 10° |
| 51° | 9.5° | 340° | 9.0° | 12° |
| 51° | 4.4° | 136° | 7.0° | 12° |
| 55° | 6.2° | 157° | 7.6° | 20° |
| 55° | 5.3° | 342° | 6.9° | 20° |
| 57° | 5.5° | 152° | 5.7° | 24° |
| 58° | 7.4° | 158° | 8.1° | 26° |
| 58° | 6.9° | 156° | 7.0° | 26° |
| 59° | 8.5° | 173° | 8.9° | 28° |
| 59° | 4.6° | 148° | 5.1° | 28° |
| 60° | 7.3° | 165° | 5.1° | 30° |
| 61° | 8.9° | 164° | 7.4° | 32° |
| 62° | 11.9° | 330° | 10.5° | 34° |
| 62° | 6.9° | 330° | 7.2° | 34° |
| 63° | 10.3° | 344° | 8.9° | 36° |
| 65° | 9.9° | 339° | 8.6° | 40° |
| 66° | 4.8° | 156° | 7.3° | 42° |
| 69° | 5.5° | 147° | 6.0° | 48° |
| 72° | 8.4° | 332° | 8.8° | 54° |

[a]Dip direction is in degrees east of north. These fault orientations are also plotted in Figure 8. The angle of internal friction, $\phi$, is calculated from the value of dip using equation (1).

**Table 1b.** Measurements of Dip, Dip Direction, and Corresponding Errors for Thrust Faults in the Study Area[a]

| Dip | Error | Dip Direction | Error | $\phi$ |
|---|---|---|---|---|
| 17° | 4.7° | 124° | 6.9° | 56° |
| 17° | 10.1° | 328° | 9.1° | 56° |
| 18° | 6.4° | 144° | 6.5° | 54° |
| 18° | 6.1° | 202° | 7.2° | 54° |
| 21° | 6.6° | 247° | 7.2° | 48° |
| 22° | 7.9° | 89° | 6.6° | 46° |
| 23° | 3.4° | 156° | 6.4° | 44° |
| 24° | 11.9° | 332° | 9.1° | 42° |
| 24° | 8.3° | 325° | 6.8° | 42° |
| 24° | 9.5° | 151° | 8.1° | 42° |
| 24° | 5.2° | 337° | 9.0° | 42° |
| 27° | 7.2° | 158° | 6.4° | 36° |
| 27° | 7.3° | 359° | 8.2° | 36° |
| 27° | 5.8° | 75° | 7.1° | 36° |
| 28° | 5.5° | 238° | 7.2° | 34° |
| 29° | 7.5° | 105° | 6.9° | 32° |
| 30° | 6.0° | 167° | 5.7° | 30° |
| 31° | 5.6° | 138° | 7.1° | 28° |
| 31° | 7.8° | 147° | 7.3° | 28° |
| 31° | 4.4° | 331° | 6.7° | 28° |
| 34° | 7.9° | 2° | 7.7° | 22° |
| 35° | 4.7° | 337° | 7.2° | 20° |
| 35° | 6.5° | 337° | 5.7° | 20° |
| 36° | 4.0° | 152° | 6.7° | 18° |
| 36° | 10.4° | 181° | 9.9° | 18° |
| 38° | 5.8° | 43° | 5.9° | 14° |
| 39° | 4.2° | 346° | 4.8° | 12° |
| 40° | 6.3° | 88° | 7.5° | 10° |

[a]Dip direction is in degrees east of north. These fault orientations are also plotted in Figure 8. The angle of internal friction, $\phi$, is calculated from the value of dip using equation (1).

and no evidence of attendant growth folds [e.g., *Sharp et al.*, 2000], within the local ILD. Thus deposition of these ILD in a preexisting basin is most consistent with the observed bedding orientations. Accordingly, basinward creep of the ILD, triggered by chasma subsidence, is not likely to have influenced the observed layer orientations either.

[34] Results of our structural mapping therefore reveal lines of evidence that support the interpretation that the ILD exposed within the study area were deposited after any chasma-forming normal faulting had occurred in this part of Candor Chasma. Normal faults of adequate length and orientation are not observed in the local ILD. Thus if chasma-related normal faulting occurred in the study area, it must predate deposition of the local ILD exposed at the surface. Additionally, the adjacent catena, which may be genetically related to chasma formation, are not observed to deform the ILD locally. Thus these catena, and underlying fractures, must either predate these ILD or not extend into southwest Candor Chasma. Further, observed bedding orientations are most consistent with deposition of the local ILD as basin-filling sediments. These independent lines of evidence are interpreted to indicate that the ILD exposed in the study area were deposited within a preexisting basin that evolved into the present-day Candor Chasma independent of any subsequent chasma-related normal faulting. This finding is consistent with interpretations that deposition of ILD continued after the chasma had formed [e.g., *Komatsu et al.*, 1993; *Schultz*, 1991, 1998a; *Lucchitta*, 1990; *Lucchitta et al.*, 1992; *Weitz et al.*, 2001]. More specifically, this finding supports interpretations that west Candor Chasma formed as an ancestral basin that was subsequently filled by ILD, and that subsequent rifting in Candor was focused in the northeast part of the chasma [*Lucchitta and Bertolini*, 1989; *Lucchitta et al.*, 1994].

[35] Since the faults generally postdate large-scale folding, measurements of fault dip are regarded to be largely representative of dip of the fault as it propagated. Therefore these measurements of fault dip can be used to estimate the angle of internal friction of the local ILD. Fault orientation, $\theta_f$, is related to the rock mass' angle of internal friction, $\varphi_f$, through [*Jaeger and Cook*, 1979]

$$\theta_f = 45^\circ + \frac{\phi_f}{2}. \quad (1)$$

Fault orientation, $\theta_f$, is the angle between the most compressive principal stress and the normal to the optimally oriented plane for frictional slip. Assuming that these faults propagated along planes that are optimally oriented (most favorable) for Coulomb slip and that lithostatic load acted as a principal stress in an Andersonian stress state for faulting [*Anderson*, 1951], $\theta_f = \theta_{dip}$ for normal faults and $\theta_f = 90 - \theta_{dip}$ for thrust faults, where $\theta_{dip}$ is the dip of the optimally oriented fault plane.

[36] Using equation (1), a median friction angle of 31°, with a standard deviation of 14°, is calculated for the angles of fault dip listed in Tables 1a and 1b. These median values are generally larger than previous estimates of *ca.* 5° to 18° for ILD elsewhere in Valles Marineris gathered from back calculations of slope failures [*Schultz*, 2002]. These angles of friction are consistent however with laboratory measurements of intact rock [e.g., *Byerlee*, 1978], as well as moderately weathered and fractured rock masses [e.g., *Hoek and Brown*, 1997]. Eight of the 57 fault dip measurements are found to be incongruous with the above assumptions because they were either less than 45° for normal faults, or greater than 45° for thrust faults. These measurements are excluded from the above statistic and may be due to stress interactions with adjacent faults or slipping bedding planes [e.g., *Roering et al.*, 1997; *Okubo and Schultz*, 2006].

[37] The present-day exposures of faults and folds enable the key structural measurements that are the basis of this paper. These exposures however, are not taken to be the representative of the ground surface that was present during active deformation. Several morphologic observations indicate that the present-day exposures have been exhumed through erosion. The numerous folds that are present within the study area have apparently been eroded into, such that their subsurface (internal) structure is now exposed (e.g., Figures 4a and 4b). Additionally, slip along normal faults and thrust faults at depth results in the formation of fault-related folds, and occasionally pit craters, at the surface [e.g., *Mitra*, 1990; *Sharp et al.*, 2000; *Martel and Langley*, 2006]. These telltale surficial structures are not preserved in the study area. Instead, only fault planes are apparent. This is interpreted to be the result of erosion and removal of the ground surface, and any fault-related structure, that was present during active deformation. Therefore the present-day exposures provide windows into the subsurface structure of these faults and folds, and these structures do not reflect an active or recent stage of deformation. Eolian

activity is likely to be the most recent pervasive erosional process given the abundance of eolian features (e.g., sand dunes) and the lack of fluvial landforms.

[38] While the spatial distribution of the faults and folds does not support interpretations of chasma-related normal faulting, this pattern of strain is consistent with the subsurface structure of a landslide [e.g., *Cruden and Varnes*, 1996]. The normal faults may represent failure in the headscarp region of a slide, and the thrust faults and the F2 folds may reflect compression at the toe. The amount of displacement of the local ILD is not so large as to completely disrupt bedding throughout the study area, except in the putative toe region where these ILD are fragmented by thrust faults. Thus such a landslide may be classified as a slump. In this way, the observed faults and folds may represent a subaerial or subaqueous landslide that has been sufficiently eroded such that the characteristic surface morphology is no longer present. The observed southward vergence of the landslide features (faults and folds; Figure 8) is consistent with mass movement along a south-facing slope. Since this landslide is located on a south-facing slope at present (Figure 7), we propose that the slide occurred when the local topography of the ILD was similar to that of the present-day.

[39] Landslides of other ILD material have been previously identified in areas such as here in west Candor Chasma [*Lucchitta*, 2000; *Chapman and Tanaka*, 2001] location Z in Figure 1 and in east Candor Chasma [*Neuffer and Schultz*, 2006], as well as in Melas and Hebes Chasmata [*Skilling et al.*, 2002; *Weitz et al.*, 2003; *Neuffer and Schultz*, 2006]. Thus present-day exposures through deeper levels of such slides can be expected if erosion is sufficiently pervasive. Therefore the apparent scarcity of landslides elsewhere in the ILD [e.g., *Lucchitta*, 1987; *Nedell et al.*, 1987] may be due to erosion of characteristic mass wasting morphologies, which would make these features difficult to identify in low-resolution imagery. Ongoing mapping of adjacent sections of the DTM, the overlapping CTX image and an adjacent HiRISE DTM will help to further develop these preliminary interpretations.

[40] On the basis of these preceding observations, the following geologic history of the study area is proposed. The Tithonia Catenae form, possibly in response to dikes that are radial to Syria Planum [e.g., *Mège and Masson*, 1996]. The Candor ancestral basin then forms and ILD accumulates within it [e.g., *Lucchitta et al.*, 1994]. Chasma-related normal faulting [e.g., *Schultz and Lin*, 2001; *Wilkins et al.*, 2002] and contemporaneous erosion of older ILD may have occurred in the study area around this time. If chasma-related normal faulting and erosion did occur, the ILD currently exposed in the study area would have been deposited after these events. The F1 folds then begin to form, accommodating shortening in a northeast-southwest direction. Normal faulting, thrust faulting, and F2 folding subsequently occur, marking an eventual change to a northwest-southeast shortening direction. This second stage of deformation results in a net movement of material toward the southeast. Deformation along the folds and faults eventually ceases, and eolian erosion creates in the present-day exposures. Accordingly, the observed deformation is not found to be directly related to chasma formation, but instead may be due in part to slumping of the local ILD. Deposition of the local ILD on a preexisting (e.g., erosional) slope of older ILD could have driven this deformation through landslide processes.

[41] While insightful, the results from this relatively small study area present only a glimpse into the broader geologic history of the ILD in west Candor Chasma. In order to build a more comprehensive picture of faulting and folding here, future work will focus on gathering additional structural information from adjacent HiRISE DEMs. Results of these and additional studies from other high-resolution data sets (e.g., HRSC), can then be tied together by establishing regional stratigraphic correlations at comparably high resolutions between these disparate study areas.

## 5. Summary and Conclusions

[42] High-resolution DTMs generated from stereo HiRISE imagery reveal the meter-scale structure of the ILD in the study area, located in southwest Candor Chasma. These observations show that while normal faults are observed within the local ILD, these faults are not sufficiently large, nor appropriately oriented to accommodate the northeast-southwest extension that is required for normal faults that can be attributed to chasma formation. Additionally, bedding in these ILD generally dips toward the center of Candor Chasma, consistent with sediment deposition in a preexisting basin. Further, pit craters of Tithonia Catena, presumed to predate or to be contemporaneous with the formation of west Candor Chasma, do not cut into the ILD within the study area. These independent lines of evidence support a postchasma age for the ILD within the study area. Older, faulted ILD may exist at depth, but are not exposed in the study area. An approximately 2 km thick stratigraphic sequence is exposed throughout the area studied here. Therefore at least several kilometers of ILD were deposited in this part of Candor Chasma subsequent to any chasma-related normal faulting.

[43] **Acknowledgments.** The authors acknowledge the contributions of the science and operations teams for HiRISE and MRO, without whom this work would not be possible. We thank Frank Fueten and Daniel Mège for comments that helped to improve this paper. This work is supported by a grant from NASA's Mars Data Analysis Program to C. H. Okubo (NNX06AE01G).

## References

Anderson, E. M. (1951), *The Dynamics of Faulting and Dyke Formation, with Applications to Britain*, 206 pp., Oliver and Boyd, Edinburgh, U. K.

Anguita, F., A.-F. Farelo, V. López, C. Mas, M.-J. Muñoz-Espadas, A. Márquez, and J. Ruiz (2001), Tharsis dome, Mars: New evidence for Noachian-Hesperian thick-skin and Amazonian thin-skin tectonics, *J. Geophys. Res.*, *106*, 7577–7590, doi:10.1029/2000JE001246.

Byerlee, J. (1978), Friction of rocks, *Pure Appl. Geophys.*, *116*, 615–626, doi:10.1007/BF00876528.

Catling, D. C., S. E. Wood, C. Leovy, D. R. Montgomery, H. M. Greenberg, C. R. Glein, and J. M. Moore (2006), Light-toned layered deposits in Juventae Chasma, Mars, *Icarus*, *181*, 26–51, doi:10.1016/j.icarus.2005.10.020.

Chapman, M. G., and K. L. Tanaka (2001), Interior trough deposits on Mars: Subice volcanoes?, *J. Geophys. Res.*, *106*, 10,087–10,100, doi:10.1029/2000JE001303.

Cruden, D. M., and D. J. Varnes (1996), Landslide types and processes, in *Landslides: Investigation and Mitigation*, edited by A. K. Turner and R. L. Schuster, pp. 36–75, Natl. Acad. Press, Washington, D. C.

Fueten, F., R. M. Stesky, and P. MacKinnon (2005), Structural attitudes of large scale layering in Valles Marineris, Mars, calculated from Mars Orbiter Laser Altimeter data and Mars Orbiter Camera imagery, *Icarus*, *175*, 68–77, doi:10.1016/j.icarus.2004.11.010.

Fueten, F., R. Stesky, P. MacKinnon, E. Hauber, K. Gwinner, F. Scholten, T. Zegers, and G. Neukum (2006), A structural study of an interior layered deposit in southwestern Candor Chasma, Valles Marineris, Mars, using high-resolution stereo camera data from Mars Express, *Geophys. Res. Lett.*, *33*, L07202, doi:10.1029/2005GL025035.

Fueten, F., R. Stesky, P. MacKinnon, E. Hauber, K. Gwinner, F. Scholten, T. Zegers, G. Neukum, and the HRSC Co-Investigator Team (2007), Faulting of ILD deposits on Ceti Mensa, western Candor Chasma, Mars, *Lunar Planet. Sci.*, *XXXVIII*, abstract 1388.

Fueten, F., R. Stesky, P. MacKinnon, E. Hauber, K. Gwinner, F. Scholten and T. Zegers (2008), Structural relations of a sulfate-bearing unit near Ceti Mensa, Candor Chasma, Mars, *Lunar Planet. Sci.*, *XXXIX*, abstract 1428.

Hamelin, N., H. Racher, F. Fueten, R. Stesky, P. MacKinnon, E. Hauber, K. Gwinner, F. Scholten, and T. Zegers (2008), Structural analysis of an interior layered deposit in northern Coprates Chasma, Mars, *Lunar Planet. Sci.*, *XXXIX*, abstract 1424.

Hauber, E., et al. (2006), An integrated study of interior layered deposits in Hebes Chasma, Valles Marineris, Mars, using MGS, MO, and MEX data, *Lunar Planet. Sci.*, *XXXVII*, abstract 2022.

Hauber, E., E. Charalambakis, K. Gwinner, M. Knapmeyer, and M. Grott (2007), Displacement-length relationships of normal faults on Mars: New observations with MOLA and HRSC, paper presented at 7th International Conference on Mars, Lunar and Planet. Inst., Pasadena, Calif., 9–13 Jul.

Hoek, E., and E. T. Brown (1997), Practical estimates of rock mass strength, *Int. J. Mech. Min. Sci. Geomech. Abstr.*, *34*, 1165–1186, doi:10.1016/S0148-9062(97)00305-7.

Hynek, B. M., R. J. Phillips, and R. E. Arvidson (2003), Explosive volcanism in the Tharsis region: Global evidence in the Martian geologic record, *J. Geophys. Res.*, *108*(E9), 5111, doi:10.1029/2003JE002062.

Jaeger, J. C., and N. G. W. Cook (1979), *Fundamentals of Rock Mechanics*, 3rd ed., 593 pp., Chapman and Hall, New York.

Kirk, R. L., et al. (2008), Ultra-high-resolution topographic mapping of Mars with MRO HiRISE stereo images: Meter-scale slopes of candidate Phoenix landing sites, *J. Geophys. Res.*, *113*, E00A24, doi:10.1029/2007JE003000.

Komatsu, G., P. E. Geissler, R. G. Strom, and R. B. Singer (1993), Stratigraphy and erosional landforms of layered deposits in Valles Marineris, Mars, *J. Geophys. Res.*, *98*, 11,105–11,121, doi:10.1029/93JE00537.

Komatsu, G., G. G. Ori, P. Ciarcelluti, and Y. D. Litasov (2004), Interior layered deposits of Valles Marineris, Mars: Analogous subice volcanism related to Baikal Rifting, Southern Siberia, *Planet. Space Sci.*, *52*, 167–187, doi:10.1016/j.pss.2003.08.003.

Lucchitta, B. K. (1987), Valles Marineris, Mars: Wet debris flows and ground ice, *Icarus*, *72*, 411–429, doi:10.1016/0019-1035(87)90183-7.

Lucchitta, B. K. (1990), Young volcanic deposits in the Valles Marineris, Mars, *Icarus*, *86*, 476–509, doi:10.1016/0019-1035(90)90230-7.

Lucchitta, B. K. (1999), Geologic map of Ophir and central Candor Chasmata (MTM–05072) of Mars, *U.S. Geol. Surv. Misc. Invest. Map*, *I-2568*.

Lucchitta, B. K. (2000), New observations inside the Valles Marineris, Mars, *Lunar Planet. Sci.*, *XXXI*, abstract 1139.

Lucchitta, B. K. (2008), HiRISE images of layered deposits in west Candor Chasma, Mars (I): Wall rock relations, enigmatic ridges, and possible dikes, *Lunar Planet. Sci.*, *XXXIX*, abstract 2169.

Lucchitta, B. K., and L. M. Bertolini (1989), Interior structures of Valles Marineris, in *Proceedings of the 20th Lunar and Planetary Science Conference*, pp. 590–591, Lunar and Planet. Sci. Inst., Houston, Tex.

Lucchitta, B. K., A. S. McEwen, G. D. Clow, P. E. Geissler, R. B. Singer, R. A. Schultz, and S. W. Squyres (1992), The canyon system on Mars, in *Mars*, edited by H. H. Kieffer et al., pp. 453–492, Univ. of Ariz. Press, Tucson.

Lucchitta, B. K., N. Isbell, and A. Howington-Kraus (1994), Topography of Valles Marineris: Implications for erosional and structural history, *J. Geophys. Res.*, *99*, 3783–3798, doi:10.1029/93JE03095.

Malin, M. C., and K. S. Edgett (2000), Sedimentary rocks of early Mars, *Science*, *290*, 1927–1937, doi:10.1126/science.290.5498.1927.

Malin, M. C., and K. S. Edgett (2001), Mars Global Surveyor Mars Orbiter Camera: Interplanetary cruise through primary mission, *J. Geophys. Res.*, *106*, 23,429–23,570, doi:10.1029/2000JE001455.

Malin, M. C., et al. (2007), Context Camera Investigation on board the Mars Reconnaissance Orbiter, *J. Geophys. Res.*, *112*, E05S04, doi:10.1029/2006JE002808.

Mangold, N., A. Gendrin, B. Gondet, S. LeMouelic, C. Quantin, V. Ansan, J.-P. Bibring, Y. Langevin, P. Masson, and G. Neukum (2008), Spectral and geological study of the sulfate-rich region of West Candor Chasma, Mars, *Icarus*, *194*, 519–543, doi:10.1016/j.icarus.2007.10.021.

Martel, S. J., and J. S. Langley (2006), Propagation of normal faults to the surface in basalt, Koae fault system, Hawaii, *J. Struct. Geol.*, *28*, 2123–2143, doi:10.1016/j.jsg.2005.12.004.

McEwen, A. S., et al. (2007), Mars Reconnaissance Orbiter's High-Resolution Imaging Science Experiment (HiRISE), *J. Geophys. Res.*, *112*, E05S02, doi:10.1029/2005JE002605.

Mège, D., and P. L. Masson (1996), A plume tectonics model for the Tharsis province, Mars, *Planet. Space Sci.*, *44*(12), 1499–1546, doi:10.1016/S0032-0633(96)00113-4.

Mitra, S. (1990), Fault-propagation folds; geometry, kinematic evolution, and hydrocarbon traps, *AAPG Bull.*, *74*, 921–945, doi:10.1306/44B4B680-170A-11D7-8645000102C1865D.

Montgomery, D. R., and A. Gillespie (2005), Formation of Martian outflow channels by catastrophic dewatering of evaporite deposits, *Geology*, *33*, 625–628, doi:10.1130/G21270.1.

Nedell, S. S., S. W. Squyres, and D. W. Andersen (1987), Origin and evolution of the layered deposits in the Valles Marineris, Mars, *Icarus*, *70*, 409–414, doi:10.1016/0019-1035(87)90086-8.

Neuffer, D. P., and R. A. Schultz (2006), Mechanisms of slope failure in Valles Marineris, Mars, *Q. J. Eng. Geol. Hydrogeol.*, *39*, 227–240, doi:10.1144/1470-9236/05-042.

Okubo, C. H., and R. A. Schultz (2005), Evolution of damage zone geometry and intensity in porous sandstone: Insight from strain energy density, *J. Geol. Soc.*, *162*, 939–949, doi:10.1144/0016-764904-148.

Okubo, C. H., and R. A. Schultz (2006), Near-tip stress rotation and the development of deformation band stepover geometries in mode II, *Geol. Soc. Am. Bull.*, *118*, 343–348.

Okubo, C. H., R. A. Schultz, M. A. Chan, G. Komatsu, and the HiRISE Team (2008), Deformation band clusters on Mars and implications for subsurface fluid flow, *Geol. Soc. Am. Bull.*, in press.

Peulvast, J. P., and P. L. Masson (1993a), Erosion and tectonics in central Valles Marineris (Mars): A new morpho-structural model, *Earth Moon Planets*, *61*, 191–217, doi:10.1007/BF00572245.

Peulvast, J.-P., and P. L. Masson (1993b), Melas Chasma: Morphology and tectonic patterns, *Earth Moon Planets*, *61*, 219–248, doi:10.1007/BF00572246.

Peulvast, J.-P., D. Mège, J. Chiciak, F. Costard, and P. Masson (2001), Morphology, evolution, and tectonics of Valles Marineris wallslopes (Mars), *Geomorphology*, *37*, 329–352, doi:10.1016/S0169-555X(00)00085-4.

Ramsay, J. G., and M. I. Huber (1987), *Folds and Fractures*, 2nd ed., 462 pp., Academic, London.

Roering, J. J., M. L. Cooke, and D. D. Pollard (1997), Why blind thrust faults do not propagate to the Earth's surface: Numerical modeling of coseismic deformation associated with thrust-related anticlines, *J. Geophys. Res.*, *102*, 11,901–11,912, doi:10.1029/97JB00680.

Schultz, P. H., and A. B. Lutz (1988), Polar wandering of Mars, *Icarus*, *73*, 91–141, doi:10.1016/0019-1035(88)90087-5.

Schultz, R. A. (1991), Structural development of Coprates Chasma and western Ophir Planum, central Valles Marineris rift, Mars, *J. Geophys. Res.*, *96*, 22,777–22,792, doi:10.1029/91JE02556.

Schultz, R. A. (1998a), Geologic map of MTM-10067 quadrangle of the western Coprates Chasma region of Mars, *U.S. Geol. Surv. Misc. Invest. Map*, *I-2588*.

Schultz, R. A. (1998b), Multiple-process origin of Valles Marineris basins and troughs, *Mars, Planet. Space Sci.*, *46*, 827–829, doi:10.1016/S0032-0633(98)00030-0.

Schultz, R. A. (2002), Stability of rock slopes in Valles Marineris, Mars, *Geophys. Res. Lett.*, *29*(19), 1932, doi:10.1029/2002GL015728.

Schultz, R. A., and J. Lin (2001), Three-dimensional normal faulting models of Valles Marineris, Mars, and geodynamic implications, *J. Geophys. Res.*, *106*, 16,549–16,566, doi:10.1029/2001JB000378.

Schultz, R. A., C. H. Okubo, and S. J. Wilkins (2006), Displacement-length scaling relations for faults on the terrestrial planets, *J. Struct. Geol.*, *28*, 2182–2193, doi:10.1016/j.jsg.2006.03.034.

Scott, D., and K. Tanaka (1986), Geologic map of the western equatorial region of Mars, *U.S. Geol. Surv. Misc. Invest. Map*, *I-1802-A*.

Sharp, I. R., R. L. Gawthorpe, J. R. Underhill, and S. Gupta (2000), Fault-propagation folding in extensional settings: Examples of structural style and synrift sedimentary response from the Suez Rift, Sinai, Egypt, *Geol. Soc. Am. Bull.*, *112*, 1877–1899, doi:10.1130/0016-7606(2000)112<1877:FPFIES>2.0.CO;2.

Skilling, I. P., M. G. Chapman, and B. K. Lucchitta (2002), Young, blocky flows in east Ius/west Melas and west Candor Chasmata, Mars: Debris avalanche deposits derived from interior layered deposit (ILD) mounds?, *Lunar Planet. Sci.*, *XXXIII*, abstract 1361.

Sowe, M., E. Hauber, R. Jaumann, K. Gwinner, F. Fueten, R. Stesky, and G. Neukum (2007), Interior layered deposits in the Eastern Valles Marineris and Chaotic Terrains on Mars, *Lunar Planet. Sci.*, *XXXVIII*, abstract 1568.

Suppe, J. (1985), *Principles of Structural Geology*, 537 pp., Prentice-Hall, Englewood Cliffs, N. J.

Tanaka, K. L., and M. P. Golombek (1989), Martian tension fractures and the formation of grabens and collapse features at Valles Marineris, in *Proceedings of the 19th Lunar and Planetary Science Conference*, pp. 383–396, Lunar and Planet. Sci. Inst., Houston, Tex.

Weitz, C. M., T. J. Parker, F. S. Anderson, and J. A. Grant (2001), The interior layered deposits of Valles Marineris: Layering, erosional processes, and age relationships, *Lunar Planet. Sci.*, *XXXII*, abstract 1629.

Weitz, C. M., T. J. Parker, M. H. Bulmer, F. Scott Anderson, and J. A. Grant (2003), Geology of the Melas Chasma landing site for the Mars Exploration Rover mission, *J. Geophys. Res.*, *108*(E12), 8082, doi:10.1029/2002JE002022.

Wilkins, S. J., and R. A. Schultz (2003), Cross faults in extensional settings: Stress triggering, displacement localization, and implications for the origin of blunt troughs at Valles Marineris, Mars, *J. Geophys. Res.*, *108*(E6), 5056, doi:10.1029/2002JE001968.

Wilkins, S. J., R. A. Schultz, R. C. Anderson, J. M. Dohm, and N. H. Dawers (2002), Deformation rates from faulting at the Tempe Terra extensional province, Mars, *Geophys. Res. Lett.*, *29*(18), 1884, doi:10.1029/2002GL015391.

Witbeck, N. E., K. L. Tanaka, and D. H. Scott (1991), The geologic map of the Valles Marineris region, Mars, *U.S. Geol. Surv. Misc. Invest. Map*, *I-2010*.

Zegers, T. E., W. Dabekaussen, E. Hauber, K. Gwinner, F. Scholten, F. Fueten, R. Stesky, P. MacKinnon, G. Neukum, and the HRSC Co-Investigator Team (2006), 3-D structural analysis of Ophir Chasma based on HRSC image data and stereo-derived DTM, *Lunar Planet. Sci.*, *XXXVII*, abstract 1605.

R. L. Kirk and C. H. Okubo, U.S. Geological Survey, 2255 North Gemini Drive, Flagstaff, AZ 86001, USA. (cokubo@usgs.gov.)

K. W. Lewis, Division of Geological and Planetary Sciences, California Institute of Technology, MC 170-25, 1200 East California Boulevard, Pasadena, CA 91125, USA.

A. S. McEwen, Lunar and Planetary Laboratory, Department of Planetary Sciences, University of Arizona, 1629 East University Boulevard, Tucson, AZ 85721, USA.